文章编号：1001-9014(2024)02-0192-08

DOI:10.11972/j.issn.1001-9014.2024.02.008

A metamaterial absorber with electrically and thermally tunable absorption frequency and absorptivity

HU Bao-Jing[1,2], HUANG Ming[2], ZHAO Jin-Yan[1], YANG Li[3*], YANG Yu-Lin[1]

(1. College of Science, Yunnan Agricultural University, Kunming 650201, China;
2. School of Information Science and Engineering, Yunnan University, Kunming 650091, China;
3. College of Big Data, Yunnan Agricultural University, Kunming 650201, China)

Abstract: A dual-tunable "perfect" metamaterial absorber composed of a "Tian-zi"-shaped bulk Dirac semimetal (BDS) resonator and strontium titanate (STO) is proposed in this work and systematically studied by performing numerical simulations. From the acquired results, it is demonstrated that the absorber can achieve 99% absorption rate at 2.613 1 THz when the BDS Fermi energy is 40 meV and the STO temperature is 400 K. Moreover, both dynamics dual-tuning of the absorption frequency and absorption rate of the absorber can be successfully achieved by varying the BDS Fermi energy level and the STO temperature. Additionally, the absorber´s performance is theoretically analyzed using both coupled mode theory (CMT) and equivalent circuit model (ECM). Finally, the changes in the absorber´s absorption spectrum are further discussed when each parameter of the model is modified, providing thus a solid theoretical basis for the design of dual-tunable filters and absorbers.

Key words: absorber, Dirac semimetal, strontium titanate, dual-tunable

吸收率和吸收频率大小电热可调的超材料吸波体

胡宝晶[1,2]，黄 铭[2]，赵金燕[1]，杨 利[3*]，杨玉林[1]

(1. 云南农业大学 理学院，云南 昆明 650201；
2. 云南大学 信息学院，云南 昆明 650091；
3. 云南农业大学 大数据学院(信息工程学院)，云南 昆明 650201)

摘要：提出了由“田”字型狄拉克半金属(BDS)谐振器和钛酸锶(STO)组成的双调谐“完美”超材料吸波体并进行数值仿真。结果表明：当BDS费米能量为40 meV、STO温度为400 K时，吸波体在2.613 1 THz处吸收率达到了99%。同时，当BDS费米能量和STO温度改变时，可实现吸波体吸收频率和吸收率大小的动态双调谐。此外，分别利用了耦合模理论(CMT)和等效电路模型(ECM)从理论上分析了吸波体的性能。最后，进一步讨论了模型各参数改变时，吸波体吸收光谱的变化规律。这为双调谐滤波器、吸波体的设计提供了理论依据。

关 键 词：吸波体；狄拉克半金属；钛酸锶；双调谐

中图分类号：TB39　　**文献标识码**：A

Introduction

Terahertz (THz) waves have attracted wide interest from the scientific community due to their comparative advantages of simultaneously possessing the characteristics of microwaves and visible light waves[1-2]. As a result, in recent years, THz absorbers have become a research hotspot in many fields[3]. However, the implementation of natural materials to achieve high-performance THz absorbers in the THz frequency range is still a huge

Received date: 2023-06-25, **revised date**: 2023-12-24　　**收稿日期**：2023-06-25，**修回日期**：2023-12-24

Foundation items: Supported by the National Natural Science Foundation of China (NSFC) (61461052, 11564044, and 61863035), Yunnan Provincial Department of Science and Technology Agricultural Joint Special Project (202101BD070001-064) and Yunnan Province Basic Research Project (202301AT070495)

Biography: HU Bao-Jing (1983-), male, Dali, associate professor, doctor. Mainly engaged in research on electromagnetic fields and microwave technology, electromagnetic metamaterials, and the design and application of related electronic devices. E-mail: 1330379709@qq.com

[*] **Corresponding author**: E-mail: yangli@stu.ynau.edu.cn

challenge due to their limitations[4]. Metamaterials are regarded as periodic composite materials with outstanding electromagnetic properties[5]. Since Landy et al. designed the first narrowband metamaterial absorber in 2008[6], the development of THz metamaterial absorbers has attained significant progress, ranging from single-band and dual-band[7] to multi-band[8] and wideband[9]. However, once most absorbers are produced, their spectral characteristics and bandwidth are difficult to be changed. Hence, their application and development are greatly limited. Therefore, the fabrication of dynamically tunable absorbers is urgently needed to fulfill the requirements of many intelligent systems.

To design absorbers with dynamic tunability, many new materials, such as semiconductors[10], vanadium dioxide[11-12], and liquid water[13] have been extensively applied in absorber research and design. However, these materials generally suffer from various disadvantages, such as low efficiency and inconvenient operation. In recent years, bulk Dirac semimetals (BDS) have been applied in the design of metamaterial absorbers[14-16]. The dielectric constant of BDS can be dynamically tuned by changing the values of the Fermi energies[17-18]. At the same time, BDSs have higher mobility, they can be easier manufactured and are more stable[19-20]. In addition to BDS, strontium titanate (STO) is also a ferroelectric material with a relatively high dielectric constant and low dielectric loss. STO′s response to terahertz waves is determined by a strong polar soft vibration mode, while its relative dielectric constant can be modulated by the local temperature distribution[21]. Due to the electrically tunable characteristics of BDS and the temperature-tunable characteristics of STO, in recent years, the development of dynamic dual-tuned absorbers by using BDS and STO has been greatly explored by the scientific community. In 2020, Xiong *et al*. [22] proposed a dual-tuned absorber composed of a BDS disk with a disconnected ring and STO. Later that year, the same authors proposed another dual-tuned absorber composed of a rose-shaped BDS resonator and STO[23]. In addition, in 2021, Wu *et al*. [24] also designed a dual-tuned absorber consisting of a mixed structure of BDS resonator and STO, in which the STO layer consisted of four arrowheads and two rings. Therefore, it can be found that the previously proposed models in the published literature of dynamic dual-tuned absorbers are very complex, which greatly increases the difficulty of subsequent device processing.

Under this perspective, in this work, a dual-tunable metamaterial absorber is proposed, which is composed of a "Tian-zi"-shaped BDS resonator and STO. First, the absorber achieves "perfect" absorption effect when the BDS Fermi energy is E_F = 40 meV and the STO temperature is T = 400 K. Second, the dynamic dual-tuning of the absorption frequency and absorption rate of the absorber can be attained by varying the BDS Fermi energy and the STO temperature. Third, the performance of the absorber is theoretically analyzed using both coupled mode theory (CMT) and equivalent circuit model (ECM). Finally, the changes in the absorber′s absorption spectrum are discussed when each parameter of the model is modified, providing hence a theoretical basis for the design of both dual-tunable filters and absorbers.

1 Dielectric constants of BDS and STO

Using Kubo formula within the framework of Random Phase Approximation (RPA), both the real and imaginary parts of the dynamic conductivity of BDS can be expressed in the long wavelength limit as follows[25-26]:

$$\mathrm{Re}\,\sigma(\Omega) = \frac{e^2}{\hbar}\frac{gk_F}{24\pi}\Omega G\left(\frac{\Omega}{2}\right) \quad , \quad (1)$$

$$\mathrm{Im}\,\sigma(\Omega) = \frac{e^2}{\hbar}\frac{gk_F}{2\pi^2}\left[\frac{4}{\pi}\left(1+\frac{\pi^2}{3}\left(\frac{T}{E_F}\right)^2\right)+ 8\Omega\int_0^{\varepsilon_c}\left(\frac{G(\varepsilon)-G(\Omega/2)}{\Omega^2-4\varepsilon^2}\right)\varepsilon d\varepsilon\right] \quad , \quad (2)$$

where $G(E) = n(-E) - n(E)$, $n(E)$ represents the Fermi-Dirac distribution function, E_F denotes the Fermi energy, $k_F = E_F/\hbar v_F$ refers to the Fermi momentum, $v_F = 10^6$ m/s stands for the Fermi velocity, $g$represents the degeneracy factor, $\varepsilon = E/E_F$, $\Omega = \hbar\omega/E_F$, and $\varepsilon_c = E_c/E_F = 3$. Furthermore, substituting $\Omega \rightarrow \Omega + j\hbar\tau^{-1}/E_F$ in Eqs. (1) and (2), where $\hbar\tau^{-1} = v_F/(k_F\mu)$ signifies the scattering rate determined by the carrier mobility μ. Hence, the dielectric constant of BDS can ultimately be expressed as follows[27-28]:

$$\varepsilon_{BDS} = \varepsilon_b + \frac{j\sigma}{\omega\varepsilon_0} \quad , \quad (3)$$

where ε_0 represents the vacuum permittivity and ε_b is an effective background dielectric constant. When g = 40 and ε_b = 1 are applied, it indicates the formation of the AlCuFe quasicrystal.

On the other hand, as a temperature-dependent material, the dielectric constant of STO in the terahertz frequency range can be expressed as follows[29-30]:

$$\varepsilon_\omega = \varepsilon_\infty + \frac{F}{\omega_0^2 - \omega^2 - j\omega\gamma} \quad , \quad (4)$$

among these, ε_∞ = 9.6 represents the high-frequency dielectric constant, ωstates the angular frequency of the incident light, and $F = 2.6\times10^6\ \mathrm{cm}^2$ is the oscillator strength that is independent of the temperature. Moreover, ω_0 and γ denote the soft mode frequency and damping factor, respectively. Through Cochran′s Law, ω_0 and γ can be expressed as follows:

$$\omega_0(T)[cm^{-1}] = \sqrt{31.2(T-42.5)} \quad , \quad (5)$$

$$\gamma(T)[cm^{-1}] = -3.3 + 0.094T \quad . \quad (6)$$

Figure 1 shows the variation of the dielectric constants of BDS and STO as a function of the incident light frequency under different Fermi energies of BDS and temperatures of STO. As can be observed in Figs. 1(a) and 1(b), BDS exhibits significant sensitivity of the dielectric constants to the Fermi energy in the studied frequency range. In Fig. 1(a), the real part of the dielectric constant of BDS gradually increases from a negative value to zero, indicating the metallic properties of BDS in this frequency range. What's more, in Fig. 1(b), the

imaginary part of the dielectric constant of BDS decreases with increasing frequency and approaches to zero, indicating a very low loss of BDS at high frequencies.

As can be seen in Figs. 1(c) and 1(d), when the temperature of STO remains constant, the real part of the dielectric constant of STO slowly increases with frequency, while the imaginary part significantly increases with frequency. Furthermore, when the temperature of STO is changed, at the same frequency, both the real and imaginary parts of the dielectric constant of STO decrease with the increasing temperature. Nonetheless, the magnitude of the real part is much larger than that of the imaginary part.

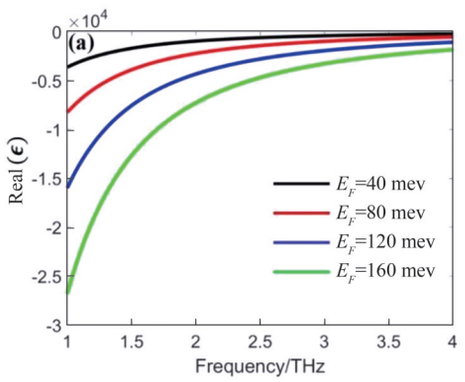

(a)

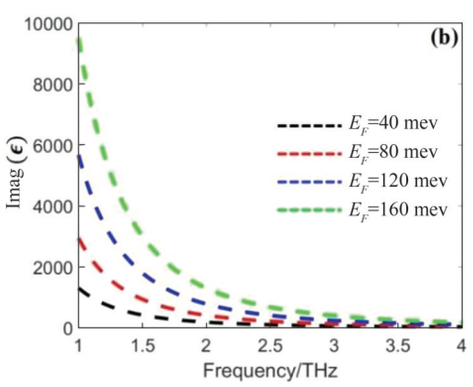

(b)

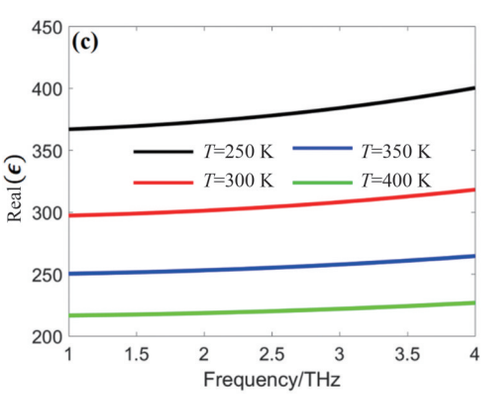

(c)

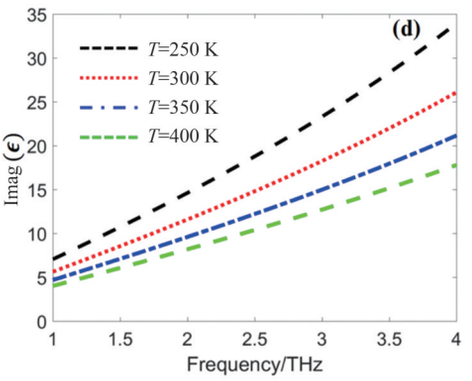

(d)

Fig. 1 The real parts (a) and imaginary parts (b) of the BDS perimittivity under different Fermi energies varying from 40 meV to 160 meV; the real parts (c) and imaginary parts (d) of the STO permittivitry under different temperatures increasing from 250 K to 400 K

图1 BDS费米能量从40 meV增加到160 meV时,BDS介电常数实部(a)和虚部(b)的变化规律;STO温度从250 K增加到400 K时,STO介电常数实部(c)和虚部(d)的变化规律

2 Model design of dual-tunable absorber and equivalent circuit model (ECM)

The three-dimensional structure of a dynamically dual-tunable absorber based on both BDS and STO is schematically illustrated in Fig. 2(a). The absorber consists of three layers: the top layer is made of a "Tian-zi" -shaped BDS nanorod resonator, the middle dielectric layer is composed of STO, and the bottom layer consists of a gold grounding layer. In Figs. 2(b) and 2(c), the length L = 2 μm, the width w = 0.2 μm, and the thickness of the top BDS "Tian-zi" -shaped nanorod h_1 = 0.2 μm, and the initial Fermi energy is 40 meV. The initial temperature and thickness of the STO layer are T = 400 K and h_2 = 2 μm, respectively. The conductivity and thickness of the gold thin film layer are $\sigma = 4.56 \times 10^7$ m/s and h_3 = 0.2 μm, respectively.

The model period is $P_x = P_y$ = 3 μm. The numerical simulation is performed by Lumerical FDTD Solutions. The background index is equal to 1. The mesh accuracy is set as 8. The periodic boundary conditions are used in both the X and Y directions, and the perfectly matched layer (PML) absorbing boundary conditions are used in the Z direction in Fig. 2(b). The incident wave is a linearly polarized wave, with the incident direction in the -Z direction and the polarization direction in the -X direction (X-polarized light). A reflective power monitor is placed above the incident wave to calculate the magnitude of reflectivity, and a transmissive power monitor is placed below the gold thin film layer to collect the date of transmittivity, respectively.

According to the transmission line theory[31-32], the equivalent circuit model (ECM) of the dual-tunable absorber is depicted in Fig. 3. In the ECM, the bottom thin film layer can be regarded as a short-circuiting de-

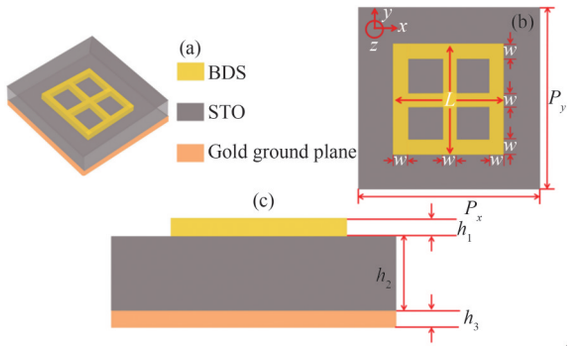

Fig. 2 Schematic designs of the dual-tunable absorber model: (a) three-dimensional view; (b) two-dimensional top view; (c) two-dimensional side view
图2 双调谐吸波体的:(a)三维结构图;(b)二维俯视图;(c)二维侧视图

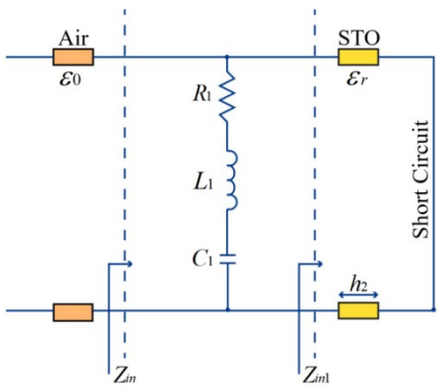

Fig. 3 The equivalent circuit model (ECM) of the proposed dual-tunable absorber
图3 双调谐吸波体的等效电路模型(ECM)

vice. At the same time, when the incident light is X-polarized light, only the nanorods in the X direction will interact with the incident light, while the nanorods in the Y direction will not interact with the incident light because the polarization direction is perpendicular to its long axis. Therefore, the top "Tian-zi" -shaped BDS nanorods can be represented by an *RLC* circuit because the three BDS nanorods in X direction have the same length.

As can be seen in Fig. 3, the input impedance of the absorber under the X-polarized light condition can be calculated as follows: $Z_{in} = 1/\left(1/Z_1 + 1/Z_{in1}\right)$, where $Z_1 = R_1 + j\omega L_1 + 1/\left(j\omega C_1\right)$ represents the equivalent impedance of the *RLC* circuit, $Z_{in1} = jZ_0 \tan\left(k_0 h_2 \sqrt{\varepsilon_r}\right) / \left(\sqrt{\varepsilon_r}\right)$ denotes the characteristic impedance of the short-circuited transmission line, Z_0 refers to the free space wave impedance, ε_r and h_2 stand for the relative permittivity and the thickness of the STO layer, and k_0 signifies the free space wave number. Therefore, under X-polarized light conditions, the reflection coefficient of the dual-tuned absorber can be expressed as follows:

$$S_{11} = \frac{Z_{in} - Z_0}{Z_{in} + Z_0} \quad . \quad (7)$$

Finally, the equivalent impedance of the dual-tuned absorber can be expressed as follows[33]:

$$Z = \sqrt{\frac{(1 + S_{11})^2 - S_{21}^2}{(1 - S_{11})^2 - S_{21}^2}} \quad . \quad (8)$$

More specifically, when the effective impedance of the absorber matches the intrinsic impedance of the vacuum, i. e., when the equivalent impedance is $Z = 1$, the reflectivity of the absorber will be zero and the absorption rate will approach to 1.

3 Absorption characteristics of absorber and coupled mode theory (CMT)

Figure 4(a) presents the extracted absorption, reflection, and transmission spectra of a double-tuned metamaterial absorber when the Fermi energy of BDS is $E_F = 40$ meV, and the temperature of STO is $T = 400$ K. The red solid line indicates that the absorber achieves the "perfect" absorption at the frequency of 2.6131 THz with an absorptivity of 99%. At the same frequency point, the reflectance of the absorber is close to zero. Additionally, throughout the entire frequency range of the analysis, the transmissivity of the absorber remains close to zero. This is because the thickness of the bottom gold thin film layer is greater than the skin depth of the incident light in the terahertz range, which can effectively block all transmissive waves and act as a reflecting layer in the model. At this point, the relationship between the absorptivity A and the reflectance R of the absorber is as follows: $A = 1 - R$.

According to Coupled Mode Theory (CMT), the physical mechanism of a "perfect" absorbing system can be described using the equation as follows[34-36]:

$$\frac{da}{dt} = \left(j\omega_0 - \frac{1}{\tau_c} - \frac{1}{\tau_a} - \frac{1}{\tau_r}\right)a + j\sqrt{\frac{2}{\tau_c}}S_+ \quad , \quad (9)$$

$$S_- = r_0 S_+ + j\sqrt{\frac{2}{\tau_c}}a \quad , \quad (10)$$

where a represents the normalized amplitude that guides the resonance, S_+ and S_- describe the normalized input and output amplitudes, respectively, whereas $1/\tau_a$ and $1/\tau_r$ denote the dissipative and radiative losses of the absorber, respectively. The strength of the coupling between the incident wave and the resonator is expressed by $1/\tau_c$. When the equivalent impedance of the absorber matches the equivalent impedance of free space, the radiative loss is $1/\tau_r = 0$. r_0 refers to the reflectance of the absorber without the BDS resonator. Since the metal layer acts as a reflecting layer in the model, all incident waves are directly reflected on the metal layer, resulting in $r_0 = -1$. Therefore, the reflectance coefficient r of the absorber can be expressed as follows:

$$r = \frac{S_-}{S_+} = \frac{j(\omega - \omega_0) + \left(\frac{1}{\tau_a} - \frac{1}{\tau_c}\right)}{j(\omega - \omega_0) + \left(\frac{1}{\tau_a} + \frac{1}{\tau_c}\right)} \quad . \quad (11)$$

Finally, the absorptivity of the absorber can be expressed as follows:

$$A = 1 - T - R = 1 - T - |r|^2 = 1 - \frac{(\omega - \omega_0)^2 + (\frac{1}{\tau_a} - \frac{1}{\tau_c})^2}{(\omega - \omega_0)^2 + (\frac{1}{\tau_a} + \frac{1}{\tau_c})^2} \quad . \quad (12)$$

As shown by the above equation, when $1/\tau_a = 1/\tau_c$, the system reflectance reaches its minimum and the absorptivity reaches its maximum at $\omega = \omega_0$. Additionally, the theoretical absorption spectrum of the CMT model is displayed in Fig. 4(b). By comparison, it can be found that the trend of the theoretical absorption spectrum is approximately consistent with the numerical absorption spectrum of FDTD.

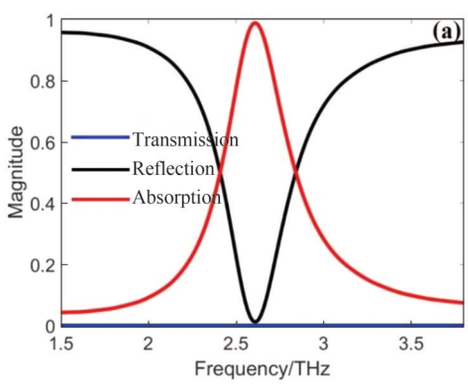

(a)

(b)

Fig. 4 (a) Simulated absorption, reflection, transmission of the designed absorber; (b) the comparison between the simulated and theoretical absorption spectrum
图4 (a)双调谐吸波体的反射、透射和吸收光谱;(b)仿真结果和CMT理论结果的比较

Figure 5 shows the electric field distribution of the absorber in the X-Y plane under X-polarized and Y-polarized conditions at the absorption peak of 2.613 1 THz. Particularly, as can be ascertained from Fig. 5(a), since only the three BDS nanorods in the X direction (indicated by the black dashed line) can directly interact with the incident light, the electric field is mainly distributed on both sides of the horizontal nanorods in a quadrupole mode. Meanwhile, by comparing Figs. 5(a) and 5(b), it can be found that the distribution of the electric field under Y-polarized conditions is mutually perpendicular to that under X-polarized conditions, and the distribution trend is approximately consistent. The electric field is mainly distributed on both sides of the three vertical nanorods (indicated by the black dashed line) in a quadrupole mode.

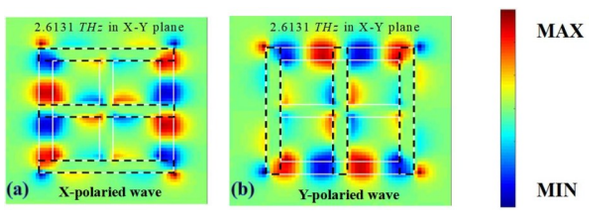

Fig. 5 The distributions of electric field at the frequency of 2.613 1 THz in the X-Y plane for (a) X-polarized wave; (b) Y-polarized wave
图5 X-Y平面中,双调谐吸波体在2.613 1 THz处的电场分布:(a)X偏振光;(b)Y偏振光

To further analyze the physical properties of the dual-tuned absorber from a theoretical point of view, Fig. 6 presents the results of the ECM analysis. As shown by Fig. 6(a), the theoretical absorption spectrum of the ECM model still matches well with the numerical absorption spectrum of FDTD. In Fig. 6(b), the equivalent impedance of the dual-tuned absorber is $Z = 1$ at the absorption frequency $f_0 = 2.613\,1$ THz, satisfying the impedance matching condition. Therefore, the absorptivity is close to 1 at this frequency.

Figure 7 illustrates the variation of the absorption spectrum of the absorber as the thickness of the BDS layer, the STO layer, and the metal layer changes. In Fig. 7(a), when the thickness of the BDS layer increases from $h_1 = 0.15$ μm to $h_1 = 0.3$ μm, the absorption frequency of the absorber slightly increases because the thickness of the BDS layer has reached a saturation value. Meanwhile, although the absorption rate slightly decreases, it remains greater than 97%[36].

As the BDS layer, the STO layer, and the metal layer in the model form an equivalent F--P resonator, the STO layer has a significant impact on the interaction between the BDS layer and the incident wave[37]. According to Fig. 7(b), as the thickness of the STO layer increases from $h_2 = 2$ μm to $h_2 = 3.5$ μm, the absorption frequency of the absorber gradually decreases, resulting in a redshift. At the same time, when the thickness of the STO layer $h_2 \leqslant 3$ μm, the absorption rate at the absorption peak remains essentially unchanged, and when $h_2 > 3$ μm, the absorption rate clearly decreases.

In Fig. 7(c), as the thickness of the metal layer increases from $h_3 = 0.05$ μm to $h_3 = 0.3$ μm, the absorption frequency and absorption rate of the absorber remain essentially unchanged. This is because although the thickness of the metal layer changes, it is always greater

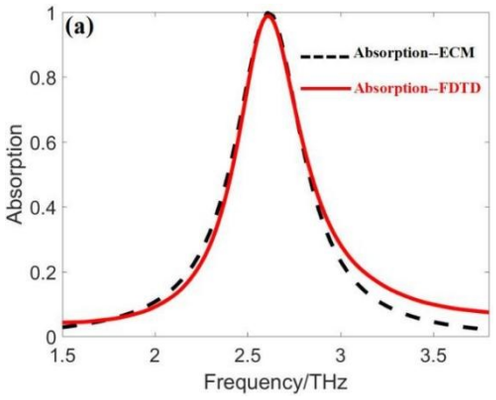

(a)

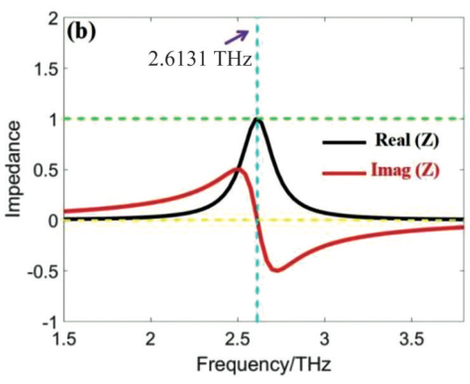

(b)

Fig. 6 (a) The comparison between the simulated absorption spectrum and the theoretical absorption spectrum analyzed by CMT; (b) the change laws of impedance of the proposed absorber under different frequencies

图 6 (a)双调谐吸波体的数值吸收率和 ECM 理论结果对比；(b)双调谐吸波体阻抗随频率的变化规律

than the skin depth of the incident light, and the transmittance of the model is always equal to 0, while the relationship between absorption rate and reflectivity remains equal to $A = 1 - R$.

Figure 8 depicts the variation of the absorption spectrum of the dual-tunable absorber with the model period p, the incident light polarization angle θ (θ is defined as the angle between the incident light polarization direction and the positive X-axis), and the length L of the BDS nanorods. As can be seen in Fig. 8(a), as the model period increases from $p = 2.5$ μm to $p = 4$ μm, the absorption frequency of the absorber slowly decreases, resulting in a red-shift.

In Fig. 8(b), due to the structural symmetry of the absorber, the absorption frequency and the absorption rate at the absorption peak remain almost unchanged as the polarization angle changes from $\theta = 0°$ to $\theta = 90°$. Therefore, with the change in the polarization angle, the absorber exhibits polarization-independent characteristics. In Fig. 8(c), as the length of the BDS nanorod increases from $L = 1$ μm to $L = 2.5$ μm, both the absorption frequency and absorption rate of the absorber's absorption spectrum remain almost unchanged.

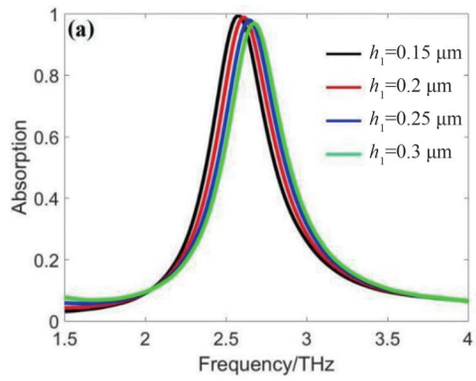

(a)

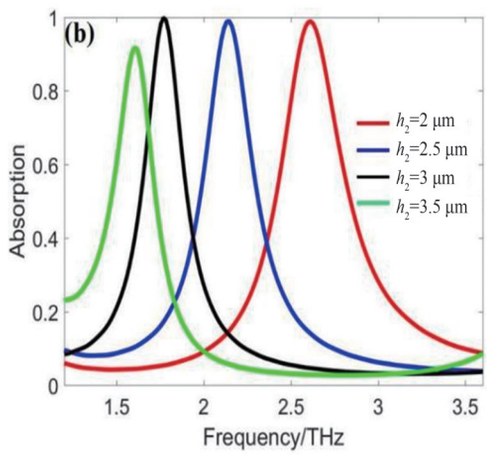

(b)

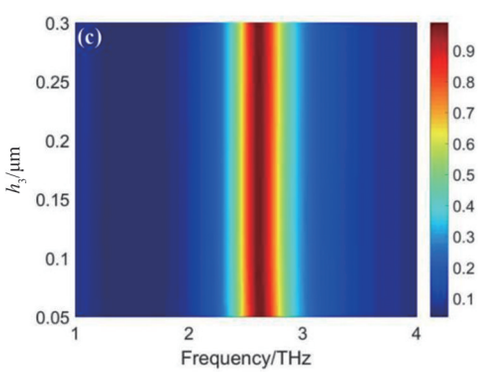

(c)

Fig. 7 Frequency dependence of absorptivity as (a) the BDS thickness increases; (b) the STO thickness increases; (c) the gold ground plane thickness increases

图 7 双调谐吸波体吸收光谱随：(a)BDS 层厚度；(b)STO 层厚度；(c)金属层厚度的变化规律

Finally, in order to verify the dynamic dual-tuning performance of the absorber, Fig. 9 presents the variation of the absorber's absorption spectrum under different

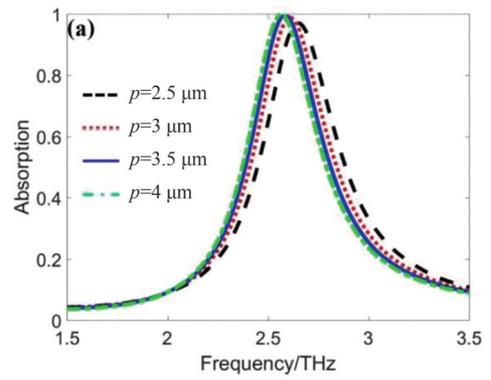

(a)

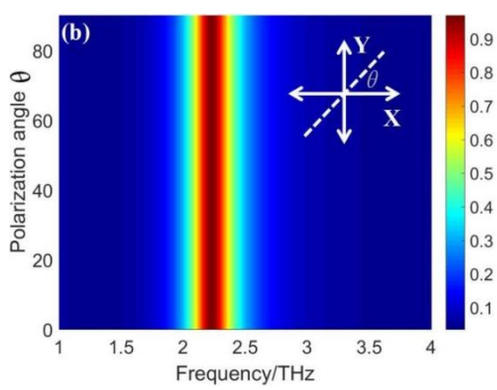

(b)

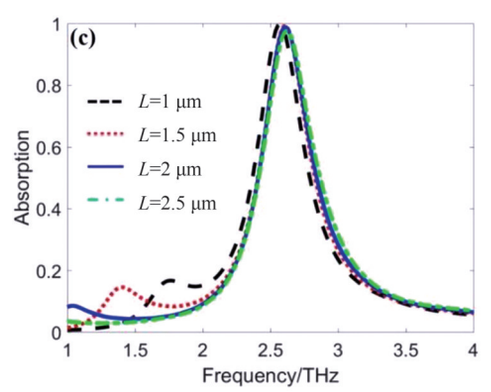

(c)

Fig. 8 Frequency dependence of absorptivity with (a) period; (b) polarization angle; (c) length of BDS rods
图8 双调谐吸波体吸收光谱随:(a)模型周期;(b)入射光偏振角;(c)BDS纳米棒长度的变化规律

BDS Fermi energies and STO temperature conditions.

As shown in Figs. 1(a) and 1(b), with the increase in the Fermi energy, the real part of the BDS permittivity gradually decreases while the imaginary part increases. According to perturbation theory[38], the decrease in the permittivity will lead to an increase in the resonance frequency. Therefore, in Fig. 9(a), as the BDS Fermi energy gradually increases from E_F = 40 meV to E_F = 160 meV, the absorption frequency of the absorber increases and exhibits a blue shift. More specifically, in Fig. 9(a), as the BDS Fermi energy increases from E_F = 40 meV to E_F = 160 meV, the absorption frequency of the absorber increases from 2.613 1 THz to 3.502 5 THz, while the absorption rate decreases from 99% to 45%.

Similarly, as shown in Figs. 1(c) and 1(d), with the increase in the temperature, both the real and imaginary parts of the STO permittivity decrease. Nevertheless, the real part is much larger than the imaginary part, and the loss generated by the model is mainly determined by the imaginary part. Therefore, as the STO temperature increases, the absorption frequency of the absorber is gradually elevated, while the absorption rate remains almost unchanged[22]. Therefore, in Fig. 9(b), as the STO temperature increases from T = 250 K to T = 400 K, the absorption frequency of the absorber increases from 1.995 THz to 2.613 1 THz, exhibiting a blue shift. The absorption rate remains above 95% throughout.

In summary, we can achieve dynamic dual-tuning of the absorption frequency and absorption rate of the absorber can be achieved by changing the BDS Fermi energy and the STO temperature.

4 Conclusions

A dual-tunable metamaterial absorber comprised of a "Tian-zi" shaped BDS resonator and STO is systematically examined in the work. First, when the BDS Fermi energy E_F = 40 meV and STO temperature T = 400 K are satisfied, the proposed absorber achieves 99% absorption at 2.613 1 THz, realizing "perfect" absorption. Second, when the STO temperature T = 400 K and the BDS Fermi energy increases from E_F = 40 meV to E_F = 160 meV, the absorption frequency of the absorber can range from 2.613 1 THz to 3.502 5 THz, and the absorption rate can decrease from 99% to 45%. Third, when the BDS Fermi energy E_F = 40 meV and STO temperature increases from T = 250 K to T = 400 K, the absorber's absorption frequency can range from 1.995 THz to 2.613 1 THz, and the absorption rate remains higher than 95%. Fourth, the performance of the absorber is theoretically analyzed using Coupling-mode theory (CMT) and Equivalent-circuit model (ECM). Finally, the variation rules of the absorber's absorption spectrum with respect to the model period, incident polarization angle, BDS rod length, thickness of BDS layer, STO layer, and metal layer are also taken into account. Our work paves the way for the design of dual-tunable filters and absorbers by providing valuable theoretical insights.

References

[1] Rappaport T S, Xing Y, Kanhere O, *et al*. Wireless communications and applications above 100 GHz: opportunities and challenges for 6g and beyond [J]. *IEEE Access*, 2019, **7**: 78729-78757.
[2] Tonouchi M. Cutting-edge terahertz technology [J]. *Nature Photonics*, 2007, **1**: 97-105.
[3] Xiong H, Wu Y B, Dong J, *et al*. Ultra-thin and broadband tunable metamaterial graphene absorber [J]. *Optics Express*, 2018, **26**(2): 1681-1688.
[4] Withawat W, Derek A. Metamaterials in the Terahertz Regime [J].

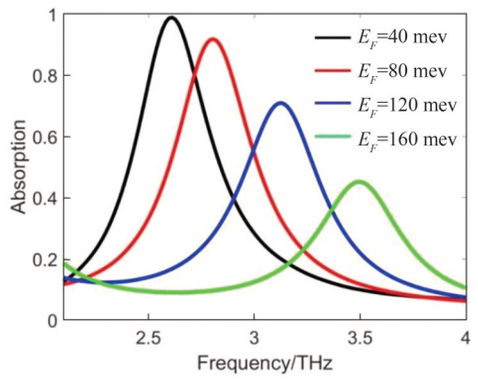

(a)

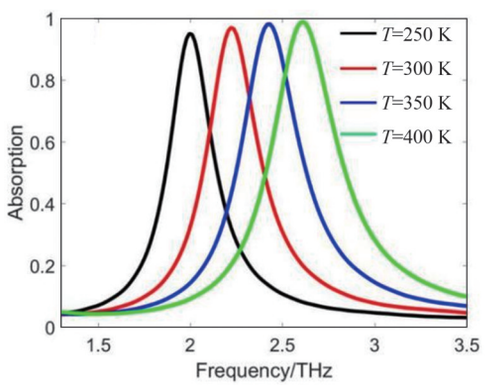

(b)

Fig. 9 (a) The change laws of absorption spectra under different Fermi energies of BDS; (b) the change laws of absorption spectra under different temperatures of STO
图9 (a)吸波体吸收率随BDS费米能量的变化规律;(b)吸波体吸收率随费米能量STO温度的变化规律

IEEE Photonics Journal, 2009, **1**(2): 99-118.
[5] Willie J, Richard D. Imaging with metamaterials [J]. *Nature Reviews Physics*, 2022, **4**: 85-100.
[6] Landy N I, Sajuyigbe S, Mock J J, *et al*. Perfect Metamaterial Absorber [J]. *Physical Review Letters*, 2008, **100**: 207402.
[7] Wang T L, Zhang H Y, Zhang Y P, *et al*. A bi-tunable switchable polarization-independent dual-band metamaterial terahertz absorber using VO2 and Dirac semimetal [J]. *Results in Physics*, 2020, **19**: 103484-103487.
[8] Hu B J, Huang M, Li P, *et al*. Dynamically dual-tunable dual-band to four-band metamaterial absorbers based on bulk Dirac semimetal and vanadium dioxide [J]. *Journal of the Optical Society of America A*, 2022, **39**: 383-391.
[9] James G, Yong M, Shimul S, *et al*. Polarization insensitive, broadband terahertz metamaterial absorber [J]. *Optics Letters*, 2011, **36** (17): 3476-3478.
[10] Zhao X G, Wang Y, Schalch J, *et al*. Optically Modulated Ultra-Broadband All-Silicon Metamaterial Terahertz Absorbers [J]. *ACS Photonics*, 2019, **6**(4): 830-837.
[11] Kocer H, Butun S, Banar B, *et al*. Thermal tuning of infrared resonant absorbers based on hybrid gold-VO2 nanostructures [J]. *Applied Physics Letters*, 2015, **106**: 161104.
[12] Song Z Y, Wang K, Li J W, *et al*. Broadband tunable terahertz absorber based on vanadium dioxide metamaterials [J]. *Optics Express*, 2018, **26**(6): 7148-7154.
[13] Xiong H, Yang F. Ultra-broadband and tunable saline water-based absorber in microwave regime [J]. *Optics Express*, 2020, **28**(4): 5306-5316.
[14] Liu G D, Zhai X, Meng H Y, *et al*. Dirac semimetals based tunable narrowband absorber at terahertz frequencies [J]. *Optics Express*, 2018, **26**(9): 11471-11480.
[15] Wang Y, Cao M, Zhang Y, *et al*. Tunable polarization-nonsensitive electromagnetically induced transparency in Dirac semimetal metamaterial at terahertz frequencies [J]. *Optical Materials Express*, 2019, **9**(4): 1562-1576.
[16] Xiong H, Ji Q, Bashir T, *et al*. Dual-controlled broadband terahertz absorber based on graphene and Dirac semimetal [J]. *Optics Express*, 2020, **28**(9): 13884-13894.
[17] Wang L X, Li C Z, Yu D P, *et al*. Aharonov - Bohm oscillations in Dirac semimetal Cd3As2 Nanowires [J]. *Nature Communications*, 2016, **7**(1): 10769.
[18] Wang Q, Wang X, Zhang L, *et al*. Tunable defect modes of one dimensional photonic crystals containing a Dirac semimetal-based metamaterial defect layer [J]. *Applied Optics*, 2019, **58** (1): 94-101.
[19] Neupane M, Xu S Y, Sankar R, *et al*. Observation of a three-dimensional topological Dirac semimetal phase in high-mobility Cd3As2 [J]. *Nature Communications*, 2014, **5**(1): 3786.
[20] Luo J, Su Y, Zhai X, *et al*. Tunable terahertz perfect absorbers with Dirac semimetal [J]. *Journal of Optics*, 2019, **21**(4): 045104.
[21] He X, Lin F, Liu F, *et al*. Tunable strontium titanate terahertz all-dielectric metamaterials [J]. *Journal Of Physics D-applied Physics*, 2020, **53**(15): 155105.
[22] Xiong H, Peng Y, Yang F, *et al*. Bi-tunable terahertz absorber based on strontium titanate and Dirac semimetal [J]. *Optics Express*, 2020, **28**(10): 15744-15752.
[23] Xiong H, Shen Q. A thermally and electrically dual-tunable absorber based on Dirac semimetal and strontium titanate [J]. *Nanoscale*, 2020, **12**(27): 14598-14604.
[24] Wu T, Sho Y B, Ma S, *et al*. Broadband terahertz absorber with tunable frequency and bandwidth by using Dirac semimetal and strontium titanate [J]. *Optics Express*, 2021, **29**(5): 7713-7723.
[25] Kotov O V, Lozovik Y E. Dielectric response and novel electromagnetic modes in three-dimensional Dirac semimetal films [J]. *Physical Review B*, 2016, **93**: 235417-235421.
[26] Zhou J, Chang H R, Xiao D, *et al*. Plasmon mode as a detection of the chiral anomaly in Weyl semimetals [J]. *Physical Review B*, 2015, **91**: 035114-035117.
[27] Zhao J X, Song J L, Zhou Y, *et al*. Tunable multiple plasmonin-duced transparency in a simple terahertz Dirac semimetal based metamaterial [J]. *Optical Materials Express*, 2019, **9**: 3325 - 3332.
[28] Wang Q, Wang X L, Zhang L W, *et al*. Tunable defect modes of one-dimensional photonic crystals containing a Dirac semimetal-based metamaterial defect layer [J]. *Applied Optics*, 2019, **58**: 94-101.
[29] Huang X, Yang F, Gao B, *et al*. Metamaterial absorber with independently tunable amplitude and frequency in the terahertz regime [J]. *Optics Express*, 2019, **27**(18): 25902-25911.
[30] Chen H, Zhang H, Liu M, *et al*. Realization of tunable plasmonin-duced transparency by bright-bright mode coupling in Dirac semimetals [J]. *Optical Materials Express*, 2017, **7**(9): 3397-3407.
[31] He X, Yao Y, Zhu Z, *et al*. Active graphene metamaterial absorber for terahertz absorption bandwidth, intensity and frequency control [J]. *Optical Materials Express*, 2018, **8**: 1031.
[32] Huang H, Xia H, Xie W, *et al*. Design of broadband graphene-metamaterial absorbers for permittivity sensing at mid-infrared regions [J]. *Scientific Report*, 2018, **8**: 4183.
[33] Smith D R, Vier D C, Koschny T, *et al*. Electromagnetic parameter retrieval from inhomogeneous metamaterials [J]. *Physical Review E*, 2005, **71**: 036617.
[34] Haus H A, Huang W P. Coupled-mode theory [J]. *PROCeedings of the IEEE*, 1991, **79**: 1505-1518.
[35] Rosolen G, Maes B. Graphene ribbons for tunable coupling with plasmonic subwavelength cavities [J]. *Journal of the Optical Society of America A*, 2014, **31**: 1096-1192.
[36] Li H, Wang L, Zhang B, *et al*. Tunable edge-mode-based mid-infrared plasmonically induced transparency in the coupling system of coplanar graphene ribbons [J]. *Applied Physics Express*, 2015, **9**: 01200.
[37] Liu M, Kang W, Zhang Y. Dynamically controlled terahertz coherent absorber engineered with VO2-integrated Dirac semimetal metamaterials [J]. *Optics Communications*, 2022, **503**: 127443.
[38] Emani N K, Kildishev AV, Shalaev V M, *et al*. A Dynamic Platform for Electrical Control of Plasmonic Resonance [J]. *Nanophotonics* 2015, **4**(1): 214-223.